Contractility-Induced Phase Separation in Active Solids

Sifan Yin[1] and L. Mahadevan[1,2,3,*]

[1]*School of Engineering and Applied Sciences, Harvard University, Cambridge, Massachusetts 02138, USA*
[2]*Department of Organismic and Evolutionary Biology, Harvard University, Cambridge, Massachusetts 02138, USA*
[3]*Department of Physics, Harvard University, Cambridge, Massachusetts 02138, USA*

Experiments over many decades are suggestive that the combination of cellular contractility and active phase separation in cell-matrix composites can enable spatiotemporal patterning in multicellular tissues across scales. To characterize these phenomena, we provide a general theory that incorporates active cellular contractility into the classical Cahn-Hilliard-Larché model for phase separation in passive viscoelastic solids. Within this framework, we show how a homogeneous cell-matrix mixture can be destabilized by activity via either a pitchfork or Hopf bifurcation, resulting in stable phase separation and/or traveling waves. Numerical simulations of the full equations allow us to track the evolution of the resulting self-organized patterns in periodic and mechanically constrained domains, and in different geometries. Altogether, our study underscores the importance of integrating both cellular activity and mechanical phase separation in understanding patterning in soft, active biosolids in both *in vivo* and *in vitro* settings.

Phase separation and its analogs, long known to be important drivers of patterning in material systems [1], are increasingly recognized as being a pervasive pattern-forming mechanism in biological systems across scales, from biomolecular condensates at the cellular scale [2,3] to tissue morphogenesis in fibroblast aggregation [4], cartilage condensation [5–8], nerve cord segmentation [9], and somitogenesis [10].

In multicellular tissues, the focus of this Letter, an experimentally well-studied case of patterning that has many signatures of phase separation is that of precartilage condensation [5–8], an integrated process involving biochemical signal regulation, cell migration, cellular contractility, and extracellular matrix (ECM) deformation. An example of this process is shown in Figs. 1(a) and 1(b) associated with the formation of tracheal cartilage rings in a mouse embryo [7]. Here, an initially homogeneous mixture of (blue) cells and (pink) ECM transitions over a few days and segregates into periodic patterns. Synthetic analogs of this using reconstituted micromasses of cells and ECM recapitulate these patterns that are accompanied by cell contractility and separation of the cell and ECM phases [11–13].

Over the past few decades, various mechanisms have been proposed to explain patterning in these systems, reviewed in [14], and fall into one of four broad categories: Turing-like mechanisms based on differential diffusion, chemotaxis-based processes that focus on cell movement in response to chemokines, differential adhesion, and differential growth. However, these theoretical attempts do not explain the salient observations of Harris *et al.* [4], reproduced many times since, which we summarize here:

(i) visible evidence for phase separation of cells from the ECM, (ii) a threshold initial fraction of contractile cell fraction (or cell population density) for the process to begin, (iii) a threshold of cell contractility before
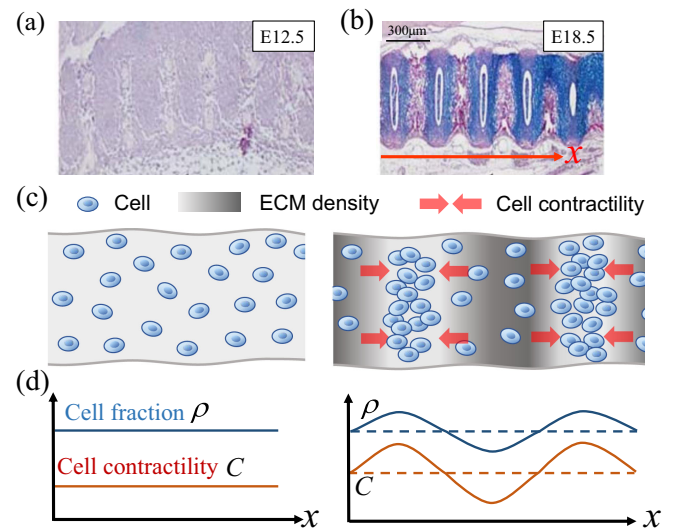

FIG. 1. Illustration of biological phase separation process. (a), (b) *In vivo* condensation of tracheal cartilage rings of mouse embryo at (a) early and (b) late stages [7]. (Scale bar: 300 μm is estimated from [11].) The blue and pink regions are mesenchymal cells and ECM, respectively. (c) Schematic of the cell-ECM mixture. Initially homogeneous soft cells (blue) scattered in ECM (gray) can contract and deform the viscoelastic biphasic mixture. Cellular contractility and movement are indicated by red arrows, and the gray color map denotes the local ECM fraction. (d) Profiles of the cell fraction ρ and active contractility C at (left) homogeneous and (right) patterned states.

condensates are initiated, and (iv) the eventual saturation of the instability to produce patterns that do not coarsen continually. An exception is the work of Oster and colleagues [5,6]; they proposed a biomechanical theory with a critical threshold for cell contractility (which we will calculate). While this can generate condensations, but they did not frame this in terms of active phase separation, for which there is now ample evidence.

Here, we generalize the Cahn-Hilliard-Larché framework [15,16] for passive phase separation, now generalized to account for active contractility. We show this schematically in Figs. 1(c) and 1(d), where cellular activity in a biphasic mixture composed of a passive but stiff ECM (gray) and scattered soft active cells (blue) can lead to phase separation when the contractility overcomes the baseline elastic resistance. We further note that unlike in classical phase separation in liquid environments that continually coarsens, here the balance between active cell contractility and the passive elastic response of the ECM eventually arrest coarsening, leading to nontrivial persistent patterns.

Active mechanical model.—We start with a consideration of isotropic two-phase systems, composed of an active phase representing mesenchymal cells that can generate active contraction and a passive phase representing ECM. We model the mixture as a viscoelastic solid capable of phase separation and deformation. This biphasic system can be described in terms of two fields that vary in space-time: the cell fraction $\rho(x, t)$ and a displacement field $\boldsymbol{u}(x, t)$. Assuming no new production of the ECM, mass conservation implies that the ECM fraction is $(1 - \rho)$. In terms of the displacement field, we can also define the velocity field $\boldsymbol{v}(x, t) = \partial_t \boldsymbol{u}(x, t)$; the strain $\boldsymbol{\varepsilon} = [\nabla \boldsymbol{u} + (\nabla \boldsymbol{u})^{\mathrm{T}}]/2$, and the strain rate $\dot{\boldsymbol{\varepsilon}} = [\nabla \boldsymbol{v} + (\nabla \boldsymbol{v})^{\mathrm{T}}]/2$. To model the combined effects of active cellular contraction, cell migration, mechanical deformation, and a thermodynamic driving force, we write the total free energy of the system as a generalization of the classical Cahn-Hilliard-Larché model for phase separation in an elastic solid [15–17] that now reads as

$$\mathcal{E}(\rho, \boldsymbol{u}) = \int_\Omega \left[g_{\mathrm{CH}}(\rho) + \frac{1}{2}\boldsymbol{\sigma}^{\mathrm{p}}(\rho, \boldsymbol{\varepsilon}, \dot{\boldsymbol{\varepsilon}}) : \boldsymbol{\varepsilon} + \boldsymbol{\sigma}^{\mathrm{a}}(\rho) : \boldsymbol{\varepsilon} \right] \mathrm{d}\boldsymbol{x}, \quad (1)$$

where $g_{\mathrm{CH}}(\rho) = \frac{1}{2}\alpha\rho^2 + \frac{1}{4}\beta\rho^4 + \frac{1}{2}\gamma|\nabla\rho|^2$ is the free energy, with $\alpha < 0$, $\beta > 0$ defining the double-well potential, and $\gamma > 0$ is the interfacial energy. The second and third terms in the expression above correspond to the mechanical strain energy due to the passive stress $\boldsymbol{\sigma}^{\mathrm{p}}$ and the work done by the active stress $\boldsymbol{\sigma}^{\mathrm{a}}$. The passive mechanical response of the ECM-cell composite is assumed to follow the Kelvin-Voigt model which for two-/three-dimensional linear viscoelastic materials reads as

$$\boldsymbol{\sigma}^{\mathrm{p}} = [2G(\rho)\boldsymbol{\varepsilon} + \lambda(\rho)\theta\boldsymbol{I}] + [2\mu_1(\rho)\dot{\boldsymbol{\varepsilon}} + \mu_2(\rho)\dot{\theta}\boldsymbol{I}], \quad (2)$$

where $\theta = \nabla \cdot \boldsymbol{u}$ is the dilatation, and $\dot{\theta} = \nabla \cdot \boldsymbol{v}$ is the dilatation rate. Here, the mechanical parameters of the mixture are the shear modulus G, first Lamé coefficient λ, shear viscosity μ_1, and bulk viscosity μ_2. Following linear mixture theory [18], the mechanical properties are taken as a weighted average of each phase—i.e., $\phi(\rho) = \phi_{\mathrm{a}}\rho + \phi_{\mathrm{p}}(1-\rho)$, where $\phi = E, \zeta, G, \lambda, \mu_1, \mu_2$, and the subscripts "a" and "p" represent the active and passive phases, respectively.

The active stress $\boldsymbol{\sigma}^{\mathrm{a}}$, which can depend on many biophysical variables is assumed to be contractile and isotropic, and of the form $\boldsymbol{\sigma}^{\mathrm{a}}(\rho) = Cf(\rho)\boldsymbol{I}$, where $C > 0$ is the contractile amplitude, and $f(\rho)$ has a saturating Hill-type functional form [19]

$$Cf(\rho) = C\frac{\rho^2}{1 + K\rho^2}, \quad (3)$$

where the contractility monotonically increases with cell fraction $\rho \in [0, 1]$ within the range $[0, C/(1 + K)]$.

Then, given the form of the active stress and the constitutive form for the solid, we may write the equations for mass and momentum balance (neglecting the effects of inertia) as

$$\partial_t \rho = -\nabla \cdot (\rho\boldsymbol{v}) + D\nabla^2 \left[\frac{\delta\mathcal{E}}{\delta\rho} \right], \quad (4)$$

$$-\frac{\delta\mathcal{E}}{\delta\boldsymbol{u}} = \nabla \cdot (\boldsymbol{\sigma}^{\mathrm{p}} + Cf(\rho)\boldsymbol{I}) = \eta\boldsymbol{v}. \quad (5)$$

Here, D is the cellular diffusivity, $\delta\mathcal{E}/\delta\rho = \mu$ is the chemomechanical potential, and η is the effective frictional coefficient associated with movement relative to a background.

Linear stability analysis.—To illustrate the essential aspects of the active biphasic system, we start with a simple one-dimensional problem [Ref. [20], Sec. II. Eq. (S4)], where the mechanical parameters are the elastic modulus E and viscosity ζ. After rescaling the governing variables using a characteristic length $\ell = \sqrt{\zeta_{\mathrm{p}}/\eta}$ and time $\tau = \zeta_{\mathrm{p}}/E_{\mathrm{p}}$, we can write the mass and force balance equations (4) and (5) as

$$\partial_t\rho = -\partial_x(\rho v) + \tilde{D}\partial_{xx}\left[\tilde{\alpha}\rho + \tilde{\beta}\rho^3 - \tilde{\gamma}\rho_{xx} \right.$$
$$\left. + \tilde{C}f'(\rho)u_x + \frac{1}{2}(\tilde{E}_{\mathrm{a}}-1)u_x^2 + \frac{1}{2}(\tilde{\zeta}_{\mathrm{a}}-1)u_xv_x \right], \quad (6a)$$

$$v = \partial_x[\tilde{E}(\rho)u_x + \tilde{\zeta}(\rho)v_x + \tilde{C}f(\rho)], \quad (6b)$$

where the dimensionless physical quantities are denoted with an upper tilde (see Ref. [20], Sec. II, Table S2). The dimensionless parameters in the model include the scaled domain size $\tilde{L} = L/\ell$, the ratio of elastic moduli
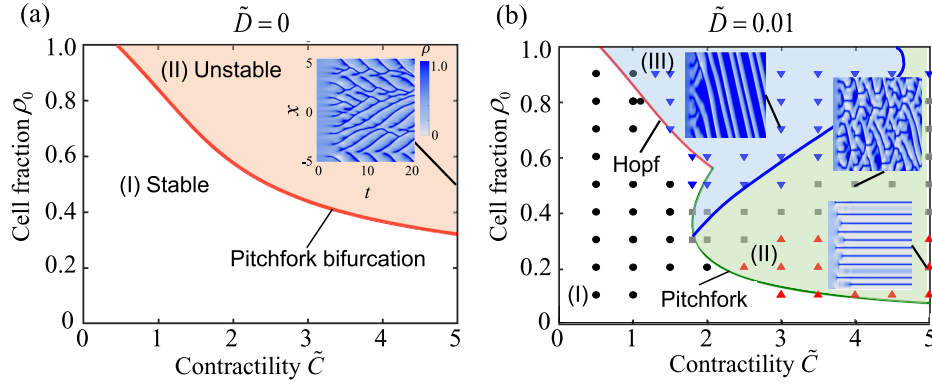
FIG. 2.   Phase diagrams in the normalized $\rho_0 - \tilde{C}$ plane obtained from linear stability analysis on a 1D model [Eq. (7)]. Colored regions depict $\mathrm{Re}(\omega) > 0$. (a) For diffusivity $\tilde{D} = 0$, pink indicates $\mathrm{Im}(\omega) = 0$ for all wave numbers. The inset shows a typical oscillatory pattern with nearly zero diffusivity $\tilde{D} = 0.0001$ [Video S1(a)], with color representing cell fraction ρ from 0 (gray) to 1 (blue), and the horizontal axis covering time $t \in [0, 20]\tau$ and the vertical axis $x \in [-5, 5]\ell$. Other parameters are $\tilde{C} = 5$ and $\rho_0 = 0.5$. (b) For nonzero diffusivity, $\tilde{D} = 0.01$, three regions are distinguished from linear stability analysis [Eq. (7)]: (I) stable (white), (II) stationary phase separation (green), and (III) oscillatory and traveling waves (blue). The white region (I) represents all the modes being stable with $\mathrm{Re}(\omega) < 0$; the green region (II) represents a finite band of modes with $\mathrm{Re}(\omega) > 0$ whereas $\mathrm{Im}(\omega) = 0$; and the blue region (III) represents a finite band of complex eigenvalues with positive real parts. Colored symbols show the systematic numerical results of the full 1D model [Eq. (6)], with periodic boundary conditions. Black dots indicate no pattern formation, red up-triangles are used for phase separation [Video S1(b)], and blue down-triangles are used for traveling waves [Video S1(c)]. Additional complex and irregular patterns (gray squares) near the interface of regions (II) and (III) are observed, which exhibit two-direction traveling and continuous fission and merging [Video S1(d)]. Three typical spatiotemporal plots of the cell fraction ρ—including traveling waves ($\tilde{C} = 3$, $\rho_0 = 0.7$), stationary phase separation ($\tilde{C} = 5$, $\rho_0 = 0.2$), and complex transition patterns ($\tilde{C} = 4$, $\rho_0 = 0.5$)—are shown in the insets, with the horizontal axis covering time $t \in [0, 100]\tau$, and the vertical axis $x \in [-5, 5]\ell$.

$\tilde{E}_a = E_a/E_p$, the ratio of viscosities $\tilde{\zeta}_a = \zeta_a/\zeta_p$, the chemical potential parameters $\tilde{\alpha}$, $\tilde{\beta}$, and $\tilde{\gamma}$, as well as the scaled diffusivity $\tilde{D} = D\eta$, and the scaled contractility $\tilde{C} = C/E_p$. Of these, the critical parameters are the last two (see Ref. [20], Sec. III A for details of the other parameters).

We next carry out a linear stability analysis of the homogeneous steady-state solutions of (6) with a uniform fraction of active cells $\rho = \rho_0$ in a stationary medium $u = v = 0$. Assuming small perturbations of the active cell fraction and displacement written as a superposition of Fourier modes $(\delta\rho, \delta u) \propto \exp[\omega_n t + ik_n x]$, where ω_n is the growth rate and $k_n = 2\pi n/\tilde{L}$ is the wave number of each mode n, we substitute these into Eqs. (6a) and (6b). This yields the dispersion relation $\omega_n = \omega(k_n^2)$ as

$$\omega(k_n^2) = \frac{1}{2a(k_n^2)}\left[-b(k_n^2) \pm \sqrt{b(k_n^2)^2 - 4a(k_n^2)c(k_n^2)}\right], \quad (7)$$

with $b(k_n^2)$ and $c(k_n^2)$ are algebraically complex functions of the wave number [Ref. [20], Sec. III. Eq. (S17)], and $a(k_n^2) = [1 + \tilde{\zeta}(\rho_o)k_n^2]/k_n^2 > 0$. We see that instability sets in when $b(k_n^2) < 0$ or $c(k_n^2) < 0$.

In the absence of diffusivity—i.e., when $\tilde{D} = 0$—increasing contractility can trigger a supercritical pitchfork bifurcation. To understand this [see Ref. [20], Sec. III, Eq. (S15)], we see that the displacement follows the simple equation $\partial_t \delta u = [\rho_0 \tilde{C} f'(\rho_0) - \tilde{E}(\rho_0)]/a(k_n^2)\delta u$. Thus, small

perturbations will decay or grow depending on the imbalance between the stabilizing elastic and destabilizing active stresses; when the scaled activity $\tilde{C} > \tilde{C}_{\mathrm{cr}} = \tilde{E}(\rho_0)/[\rho_0 f'(\rho_0)]$, the growth rate is purely real and positive for all wave numbers. We note that $\tilde{C}_{\mathrm{cr}}$ decreases monotonically with the initial (uniform) cell fraction ρ_0 [Fig. 2(a), red line]. The dominant wave number at the onset of the instability is given by [see Ref. [20], Sec. III, Eqs. (S17)–(S21)]

$$k_{\mathrm{cr}}^2 = (1/\tilde{\gamma})[\tilde{C}^2 f'(\rho_0)^2/\tilde{E}(\rho_0) - (\tilde{\alpha} + 3\tilde{\beta}\rho_0^2)]. \quad (8)$$

We see that active contraction favors small wavelengths while the elasticity prefers long wavelengths, but in either case the critical wave number is inversely proportional to the interfacial energy—i.e., $k_{\mathrm{cr}} \sim 1/\sqrt{\tilde{\gamma}}$ (see Ref. [20], Sec. V, Fig. S6).

With nonvanishing diffusivity of the active cells, either a Hopf or pitchfork bifurcation can occur. In Fig. 2(b), we see three quantitatively different regions in the phase diagram spanned by ρ_0 and $\tilde{C}$: region I is pattern-free, region II corresponds to unstable modes with purely real eigenvalues (stationary phase separation), and region III corresponds to unstable modes with complex eigenvalues (traveling waves of phase separation). Furthermore, we see that the critical contractility $\tilde{C}_{\mathrm{cr}}$ for a pitchfork bifurcation when $\tilde{D} = 0$ [see Figs. 2(a) and 2(b)] is larger than that when $\tilde{D} \neq 0$ because the driving force due to the Cahn-Hilliard chemical

potential promotes phase separation and lowers the required active contractility. However, the critical wave number for both cases is same as Eq. (8) [see Ref. [20], Sec. III A, Eqs. (S23)–(S29)].

To understand the role of material rheology on the nature of the instability, we now turn to a comparison of the purely elastic, purely viscous, and viscoelastic mixture systems. The purely viscous mixture with active contractility is always unstable via a pitchfork bifurcation, because the linear perturbation amplitude satisfies the equation $a(k_n^2)\delta u_{tt} + b(k_n^2)\delta u_t + c(k_n^2)\delta u = 0$ with $a(k_n^2) > 0$ and $c(k_n^2) < 0$, which has at least one positive real growth rate (see Ref. [20], Sec. III C). For the purely elastic and the viscoelastic mixtures, while elasticity helps to stabilize the system, contractility serves to destabilize it via either a pitchfork or a Hopf bifurcation [see Ref. [20], Fig. S3(a)]. Finally, we note that in the absence of contractility, the system only exhibits a pitchfork bifurcation associated with the classical picture of phase separation in the Cahn-Hilliard system.

Numerical simulations.—To follow the dynamics of pattern evolution beyond the onset of the instability, we numerically solved the nonlinear equations (6a) and (6b) after introducing a numerical inertia term $\Gamma\ddot{u}$ in a one-dimensional domain using a pseudospectral method [29] (spatial and temporal convergence are validated by increasing the number of collocation points and time steps [see Ref. [20], Sec. IV C, Fig. S5]) using biologically plausible parameters (see Ref. [20], Tables S1 and S2). A phase diagram for the different patterns as a function of the initial active cell fraction $\rho_a 0$ and the scaled contractility $\tilde{C}$ obtained from systematic numerical simulations shown in Fig. 2(b) agrees well with our linear instability analysis, and it goes further in describing complex dynamic behaviors away from the onset of instability.

When the diffusivity $\tilde{D} = 0$ [Fig. 2(a) inset], in the unstable region (II) we see the continuous formation and merger of bidirectional short waves of active cellular condensation [Video S1(a)], with fission and fusion statistically balancing each other. Increasing diffusivity yields three regimes, as shown in Fig. 2(b): no pattern (black dots), stationary phase separation [red up-triangles, Video S1(b)], and traveling waves [blue down-triangles, Video S1(c)]. Near the boundary of the transitions, the dynamics of patterns can be irregular and chaotic, as for example when wavefronts merge into one and then move collectively [Fig. 2(b), middle inset, Video S1(d)]. Comparing the patterns obtained from our numerical simulations with those of linear stability analysis, we find that the wavelength $\lambda = \ell$ is close to but a little smaller than the linear prediction $\lambda = 2\pi\ell/k \approx 1.4\ell$ [see Ref. [20], Fig. S2(c)]. Furthermore, the numerical characteristic width of the periodic stripe pattern (wavelength) shows $\lambda \sim \sqrt{\tilde{\gamma}}$ independent of diffusivity [see Ref. [20], Fig. S5], consistent with the linear stability analysis result given by Eq. (8).

Two-dimensional simulations exhibit more complex but qualitatively similar behaviors to those seen in our one-dimensional simulations. Using periodic boundary conditions and random initial conditions, we simulated the dynamics of Eqs. (4) and (5) [in the parameter space for phase separation, corresponding to region II in Fig. 2(b)]. Our results show how ordered and disordered spots and stripes (labyrinthine patterns) arise, similar to the experimentally observed precartilage condensation patterns in micromass cultures shown in Figs. 3(a) and 3(b) [12,30], and in Video S2. Using the parameters $\tilde{\alpha} = -1$, $\tilde{\beta} = 1$, and $\tilde{\gamma} = 0.01$–0.2, and carrying out a Fourier analysis of our simulations, yields the dominant (dimensionless) wave numbers for spots as $k_{\text{spot}} = 8.19$ in Fig. 3(a) and stripes
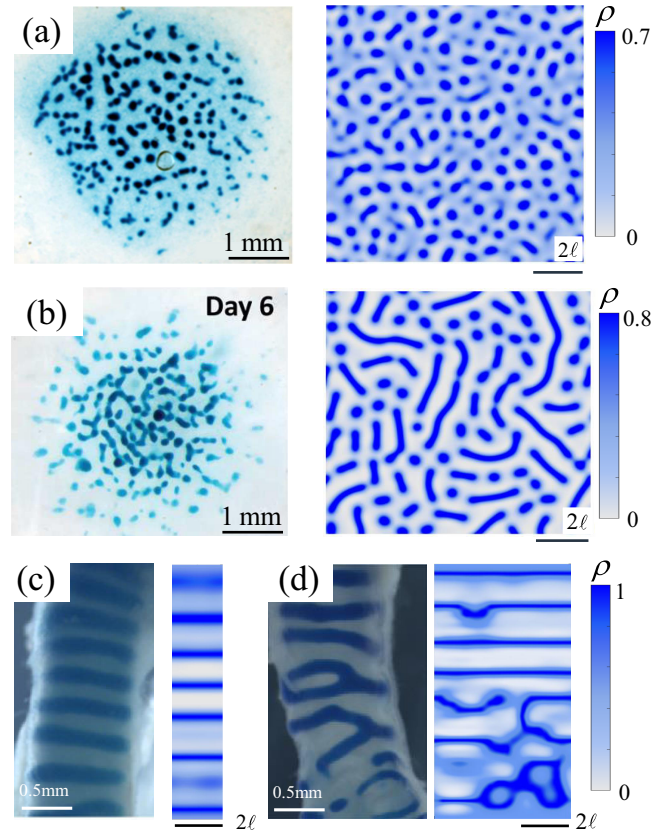

FIG. 3. Experimental and numerical simulations of representative two-dimensional dynamic patterns. (a),(b) The left column shows the images of typical *in vitro* (a) spots [12] and (b) stripes [30], patterns of precartilage condensations in micromass cultures of mesenchymal cells from mouse embryos. The right column exhibits 2D simulations of spots and labyrinth. (c),(d) Experimental (c) normal and (d) abnormal tracheal cartilage rings [8] and numerical simulations. The parameters used are (a) $\tilde{C} = 10$, $\tilde{D} = 0.001$, $\rho_0 = 0.3$, $\tilde{\gamma} = 0.01$ at $\tilde{t} = 50$, periodic BCs; (b) $\tilde{C} = 10$, $\tilde{D} = 0.01$, $\rho_0 = 0.3$, $\tilde{\gamma} = 0.01$ at $\tilde{t} = 25$, periodic BCs. Panels (c) and (d) show constant velocity $\tilde{v} = 0.001\ell/\tau$ on the top boundary with $\tilde{C} = 5$, $\tilde{D} = 0.01$, $\rho_0 = 0.5$, $\tilde{\gamma} = 0.1$, $\tilde{L}_y = 10\ell$, with $\tilde{L}_x = 2\ell$ in (c) and 5ℓ in (d). Snapshots are captured at $\tilde{t} = 100$.

as $k_{stripe} = 7.11$ in Fig. 3(b). Using experimental estimates [12,30] for $\ell \approx 0.5$ mm, we observe reasonable agreement between experimental observations and numerical results for the wavelengths of spots and stripes (see Ref. [20], Sec. V, Fig. S6).

Finally, to investigate the role of boundary conditions to understand aspects of periodic cartilage condensation along the tubular trachea in mice [8], reproduced in Figs. 3(c) and 3(d), we prescribe either a constant velocity or a constant displacement applied at the tube ends and periodic boundary conditions on the lateral boundaries associated with a cylindrical tube. Here, we neglect the effects of tube curvature by assuming that it is small relative to the wavelength of the patterns (and check that this is indeed the case later). In Fig. 3(c), we see that our simulations reproduce the experimentally observed periodic condensation patterns for low loading rates (or prescribed boundary displacements). Increasing the lateral dimensions or the rate of loading causes the pattern to become disordered as shown in Fig. 3(d) (see Ref. [20], Figs. S7 and S8).

Conclusions.—Inspired by the phase separation patterns of actively contractile cells and passive ECM mixtures in multicellular tissues, we have provided a minimal model that generalizes the classical Cahn-Hilliard-Larché theory for phase separation of elastic solids by including the effects of cell contractility as well as the viscoelastic properties (rheology) of the biphasic cell-ECM mixture. Our theory predicts a critical threshold of contractility, a critical concentration of cells and ECM for the emergence of an instability, and its eventual saturation with a finite wavelength that does not continually coarsen, consistent with observations. Our theoretical analysis of the instability and the numerical simulations provides testable predictions for the wavelength, while also accounting for the role of boundary conditions in one and two dimensions. Natural next steps include linking our theory to experiments that probe the role of activity, cell and ECM fraction and geometry of the tissue, and generalizing the theory to account for tissue growth and activity profiles that vary in space-time and are coupled to gene expression levels.

---

[*]lmahadev@g.harvard.edu

[1] A. Onuki, *Phase Transition Dynamics* (Cambridge University Press, Cambridge, England, 2002), 10.1017/CBO9780511534874.

[2] Y. Shin and C. P. Brangwynne, Science **357**, eaaf4382 (2017).

[3] A. Radja, J. Exp. Zool. B Mol. Dev. Evol. **336**, 629 (2021).

[4] A. K. Harris, D. Stopak, and P. Warner, J. Embryol. Exp. Morphol. **80**, 1 (1984), https://pubmed.ncbi.nlm.nih.gov/6747520/.

[5] G. F. Oster, J. D. Murray, and A. K. Harris, J. Embryol. Exp. Morphol. **78**, 83 (1983), https://pubmed.ncbi.nlm.nih.gov/6663234/.

[6] G. F. Oster, J. D. Murray, and P. K. Maini, J. Embryol. Exp. Morphol. **89**, 93 (1985), https://pubmed.ncbi.nlm.nih.gov/4093755/.

[7] J. Park, J. J. Zhang, R. Choi, I. Trinh, and P. C. Kim, In Vitro Cell. Dev. Biol. **46**, 92 (2010).

[8] F. G. Sala, P. M. Del Moral, C. Tiozzo, D. A. Alam, D. Warburton, T. Grikscheit, J. M. Veltmaat, and S. Bellusci, Development (Cambridge, U.K.) **138**, 273 (2011).

[9] K. Karkali, P. Tiwari, A. Singh, S. Tlili, I. Jorba, D. Navajas, J. J. Muñoz, T. E. Saunders, and E. Martin-Blanco, Dev. Cell **57**, 867 (2022).

[10] Y. Miao, Y. Djeffal, A. De Simone, K. Zhu, J. G. Lee, Z. Lu, A. Silberfeld, J. Rao, O. A. Tarazona, A. Mongera *et al.*, Nature (London) **614**, 500 (2023).

[11] S.-S. Lin, B.-H. Tzen, K.-R. Lee, R. J. H. Smith, K. P. Campbell, and C.-C. Chen, Proc. Natl. Acad. Sci. U.S.A. **111**, E1990 (2014).

[12] A. Saha, R. Rolfe, S. Carroll, D. J. Kelly, and P. Murphy, Cell Tissue Res. **368**, 47 (2017).

[13] K. H. Palmquist, S. F. Tiemann, F. L. Ezzeddine, S. Yang, C. R. Pfeifer, A. Erzberger, A. R. Rodrigues, and A. E. Shyer, Cell **185**, 1960 (2022).

[14] D. Iber and M. M., Front. Cell Dev. Biol. **10**, 900447 (2022).

[15] J. W. Cahn and J. E. Hilliard, J. Chem. Phys. **28**, 258 (1958).

[16] F. Larché and J. Cahn, Acta Metall. **21**, 1051 (1973).

[17] J. W. Cahn, Acta Metall. **9**, 795 (1961).

[18] R. M. Christensen, *Mechanics of Composite Materials* (Dover Publications, Inc., Mineola, New York, 2012).

[19] J. Murray, *Mathematical Biology II: Spatial Models and Biomedical Applications*, Interdisciplinary Applied Mathematics Vol. 18 (Springer, New York, 2003), 10.1007/b98869.

[20] See Supplemental Material at http://link.aps.org/supplemental/10.1103/PhysRevLett.131.148401 for a summary of biological background, details of linear stability analysis and numerical methods, and videos, which includes Refs. [21–28].

[21] S. Alonso, M. Radszuweit, H. Engel, and M. Bär, J. Phys. D Appl. Phys. **50**, 434004 (2017).

[22] C. Canuto, M. Y. Hussaini, A. Quarteroni, and T. A. Z. Jr., *Spectral Methods in Fluid Dynamics* (Springer, Berlin, Heidelberg, 1988).

[23] J. P. Boyd, *Chebyshev and Fourier Spectral Methods* (Springer, Dordrecht, 2000).

[24] D. A. Kopriva, *Implementing Spectral Methods for Partial Differential Equations* (Springer Science and Business Media B.V., New York, 2009).

[25] B. Hall and T. Miyake, Anat. Embryol. **186**, 107 (1992).

[26] T. Miura, M. Komori, and K. Shiota, Anat. Embryol. **201,** 419 (2000).

[27] A. J. Hughes, H. Miyazaki, M. C. Coyle, J. Zhang, M. T. Laurie, D. Chu, Z. Vavrušová, R. A. Schneider, O. D. Klein, and Z. J. Gartner, Dev. Cell **44,** 165 (2018).

[28] H. Miyazaki, Physical and cellular mechanisms underlying villus morphogenesis in the mammalian small intestine, Ph.D. thesis, University of California, San Francisco, 2021.

[29] L. N. Trefethen, *Spectral Methods in MATLAB* (SIAM, Philadelphia, 2000).

[30] N. C. Butterfield, C. Qian, and M. P. O. Logan, PLoS One **12,** e0180453 (2017).